

1 **Climatology of mesopause region nocturnal temperature, zonal wind, and sodium**
2 **density observed by sodium lidar over Hefei, China (32°N, 117°E)**

3 | Tao Li^{1*}, Chao Ban^{1,2*}, Xin Fang¹, Jing Li¹, Zhaopeng Wu¹, Wuhu Feng^{3,4}, John M. C. Plane³,
4 Jianguang Xiong⁵, Daniel R. Marsh⁶, Michael J. Mills⁶, and Xiankang Dou¹

5 ¹CAS Key Laboratory of Geospace Environment, School of Earth and Space Sciences,
6 University of Science and Technology of China, Hefei, Anhui, China

7 ²Now at Institute of Atmospheric Physics, Chinese Academy of Sciences, Beijing,
8 China³School of Chemistry, University of Leeds, Leeds, United Kingdom

9 ⁴NCAS, School of Earth and Environment, University of Leeds, Leeds, United Kingdom

10 ⁵Institute of Geology and Geophysics, Chinese Academy of Sciences, Beijing, China

11 ⁶National Center for Atmospheric Research, Boulder, CO, USA

12 | **To whom correspondence should be addressed: litao@ustc.edu.cn; banchao@mail.iap.ac.cn*

13
14 **Abstract**

15 The University of Science and Technology of China narrowband sodium temperature/wind
16 lidar, located in Hefei, China (32°N, 117°E), has made routine nighttime measurements since
17 January 2012. 154 nights (~1400 hours) of vertical profiles of temperature, sodium density,
18 and zonal wind, and 83 nights (~800 hours) of vertical flux of gravity wave (GW) zonal
19 momentum in the mesopause region (80-105 km) have been obtained during the period from
20 2012 to 2016. In temperature, it is most likely that the diurnal tide dominates below 100 km in
21 spring, while the semidiurnal tide dominates above 100 km throughout the year. A clear
22 semiannual variation in temperature is revealed near 90 km, in phase with the tropical
23 mesospheric semiannual oscillation (MSAO). The variability of sodium density is positively
24 correlated with temperature below 95 km, suggesting that in addition to dynamics, the
25 chemistry also plays an important role in the formation of sodium atoms. The seasonal
26 variability of sodium density observed by both lidar and satellite generally agrees well with a
27 whole atmosphere model simulation using an updated meteoric input function which includes
28 different cosmic dust sources. In zonal wind, the diurnal tide dominates in both spring and fall,
29 while semidiurnal tide dominates in winter. The observed semiannual variation in zonal wind
30 near 90 km is out-of-phase with that in temperature, consistent with the tropical MSAO. The
31 lidar observations generally agree with satellite and meteor radar observations as well as

Author
Moved (insertion) [1]

32 model simulations at similar latitude. The 50-70% of zonal momentum flux is induced by
33 short-period (10 min – 2 hr) GWs. The large zonal momentum flux in summer and winter due
34 to short-period GWs are clearly anti-correlated with eastward zonal wind maxima below 90
35 km, suggesting the filtering of short-period GWs by the SAO wind.

Author

Deleted: s

Author

Deleted: on the

Author

Moved up [1]: The lidar observations generally agree with satellite and meteor radar observations as well as model simulations at similar latitudes.

Author

Deleted: The GW zonal momentum flux is mostly westward in fall and winter, anti-correlated with eastward zonal wind. The annual mean flux averaged over 87-97 km is $\sim -0.3 \text{ m}^2/\text{s}^2$ (westward), anti-correlated with eastward zonal wind of $\sim 10 \text{ m/s}$.

48 1. Introduction

49 The temperature and wind in the mesopause region (80-105 km) are key atmospheric
50 parameters for studying the dynamics in this region. Ground-based instruments (e.g. lidars,
51 radars), and space-borne instruments have been widely used to measure these key parameters
52 over several decades (Vincent and Reid, 1983; She et al., 1998; Wu et al., 2008). Satellites
53 can provide a near-global view of the mesopause region, but their local coverage is usually
54 limited to two local times on the ascending and descending orbit. The lack of continuous
55 coverage in local time makes it difficult to extract information on short period gravity wave
56 (GW) perturbations from satellite data (Preusse et al., 2009). Ground-based meteor or
57 medium frequency radars are capable of measuring mesopause wind in a continuous mode,
58 but do not provide direct temperature measurements with sufficient accuracy and vertical
59 resolution (Vincent and Reid, 1983). However, a narrowband sodium lidar is able to
60 simultaneously measure mesopause region temperature and horizontal wind by utilizing the
61 sodium high resolution spectrum (She et al., 1994; Arnold and She, 2003), which provides a
62 unique opportunity to study GW perturbations and their breaking process in the mesopause
63 region (Li et al., 2005; Li et al., 2007).

64 The long-term lidar observations have been used to study the seasonal variability of
65 mesopause region temperature (She et al., 1998; Gardner et al., 2002; Xu et al., 2006;
66 Friedman et al., 2007) and horizontal wind (Franke et al., 2005; Gardner et al., 2007), as well
67 as sodium density (She et al., 2000; Gardner et al., 2005; Ejiri et al., 2010; Yi et al., 2009;
68 Yuan et al., 2012), iron density (Yi et al., 2009; Lübken et al., 2011) and potassium density
69 (Friedman et al., 2002; Plane et al., 2015). These datasets are extremely valuable to validate
70 satellite results (Xu et al., 2006; Fan et al., 2007a; Dawkins et al., 2014) and improve general
71 circulation models (Yuan et al., 2008; Feng et al., 2013; Marsh et al., 2013). When GWs
72 break or dissipate in the mesopause region due to increased amplitudes or approaching critical
73 level (where wave phase speed equal to horizontal background wind), they tend to deposit
74 wave energy and momentum into the background flow, and further modify the temperature
75 and wind near the breaking region (Lindzen et al., 1981; Liu and Hagan, 1998; Li et al., 2007).
76 Therefore, measurements of the GW vertical flux of horizontal momentum and heat are
77 critical for evaluating the GW contribution to the background state in this region, and their
78 key roles in the dynamic coupling between lower and middle/upper atmosphere (Li et al.,

79 2013; 2016).

80 The vertical flux of horizontal momentum can be directly derived from the vertical wind
81 perturbation and associated horizontal wind perturbation. To ensure accuracy of the GW
82 momentum flux, the wind data must have high temporal and vertical resolutions with good
83 precision and a long-time average (Kudeki and Franke, 1998; Thorsen et al., 2000). Several
84 studies of lidar-observed GW momentum flux in the mesosphere/lower thermosphere (MLT)
85 region have been carried out previously (Espy et al., 2004; Gardner and Liu, 2007; Acott et al.,
86 2009).

87 In this paper, we present the seasonal variation of sodium density, temperature, zonal
88 wind and GW zonal momentum flux observed by the University of Science and Technology
89 of China (USTC) sodium temperature/wind lidar from January 2012 to December 2016 over
90 Hefei, China (32°N, 117°E). This is the first time simultaneous observations of the seasonal
91 variability of mesopause region temperature, zonal wind, and GW momentum flux by sodium
92 lidar over the Eastern Asia region have been reported. We compare the lidar results with
93 temperature observed by the Sounding of the Atmosphere Using Broadband Emission
94 Radiometry (SABER) instrument onboard the Thermosphere–Ionosphere–Mesosphere
95 Energetics and Dynamics (TIMED) satellite (Russell et al., 1999); zonal wind observed by a
96 nearby meteor radar (Xiong et al., 2004); and sodium density observed by the Optical
97 Spectrograph and InfraRed Imager System (OSIRIS) onboard the Odin satellite (Llewellyn et
98 al., 2004). These measurements are then compared with simulations from the Whole
99 Atmosphere Community Climate Model version 5 (WACCM) (Marsh et al., 2013; Mills et al.,
100 2016; Feng et al., 2017), using an updated meteoric input function (MIF) for Na
101 (Cárrillo-Sánchez et al., 2016). The instruments, datasets, and data analysis method are
102 described in section 2, followed by the results of temperature and sodium density in section 3,
103 and zonal wind and GW zonal momentum flux in section 4. A summary is provided in section
104 5.

105

106 **2. Instruments, datasets and analysis method**

107 The USTC sodium temperature/wind lidar, located on campus in Hefei, China (32°N,
108 117°E), utilizes a narrowband three-frequency design and can simultaneously observe sodium
109 density, zonal wind and temperature in the mesopause region during nighttime clear sky

110 conditions (Li et al., 2012). The system was initially set up in October 2011 with two
111 receiving telescopes (30-inch diameter) pointing eastward and northward 30° from zenith for
112 measuring the zonal and meridional wind, respectively. The output laser beam is split into two
113 beams, each aligned parallel to one telescope. Between December 2012 and May 2014 (total
114 83 nights), the two receiving telescopes were pointed to eastward and westward, each 15°
115 from zenith. This dual-beam setup allows us to derive the GW zonal momentum flux as well
116 as the zonal wind. Since June 2014, the westward telescope was pointed to vertical for
117 measuring the vertical fluxes of heat and sodium atoms, and the eastward telescope to 30°
118 from zenith for measuring zonal wind. Between January 2012 and December 2016, we
119 obtained 154 nights (~1400 hours) of valid data, which is sufficient to study the seasonal
120 variations of sodium density, temperature, zonal wind, and GW momentum flux (83 nights) in
121 the mesopause region over Hefei. Figure 1 shows the number of nights with valid datasets in
122 each month of the different years. It is clear that Hefei has more clear nights in fall and winter
123 than in spring and summer.

124 The Wuhan (31°N, 114°E) meteor radar, located at ~300 km west of Hefei, has
125 measured mesopause region horizontal wind since January 2002 (Xiong et al., 2004). The
126 vertical and temporal resolutions of radar wind are 3 km and 2 hr, respectively. The SABER
127 instrument onboard the TIMED satellite can measure the near-global vertical profile of
128 temperature from the lower stratosphere to the lower thermosphere (Russell et al., 1999). The
129 SABER temperature dataset used in this paper is Level2A version 2.0, which has a vertical
130 resolution of 2 km and accuracies of ±1-2 K between 75 and 95 km, increasing to ±4 K at 100
131 km. The OSIRIS instrument onboard the Odin satellite measures solar-pumped Na resonance
132 fluorescence from a sun-synchronous polar orbit (Llewellyn et al., 2004), and the datasets can
133 be used to retrieve the global vertical profiles of sodium density between 75 and 110 km with
134 a ~10% uncertainty for 2 km vertical resolution (Gumbel et al., 2007; Fan et al., 2007a).

135 To compare with lidar results, we also use the temperature, zonal wind, and sodium
136 density simulated by the WACCM, a chemistry-climate model which extends from the
137 Earth's surface to the lower thermosphere (~140 km) (Garcia et al., 2007; Marsh et al., 2013a).
138 WACCM uses the framework from the fully coupled global climate model Community Earth
139 System Model (CESM version 1, e.g., Hurrell et al., 2013). In this paper, we use a version of
140 WACCM described in Mills et al. (2016), which includes all the detailed physical processes

Author

Deleted: 20

142 as described in the Community Atmosphere Model, version 5 (CAM5) (Neale et al., 2012).
143 The current configurations for WACCM are based on a finite volume dynamical core (Lin,
144 2004) for the tracer advection as well as a new surface topography data from Lauritzen et al.
145 (2015). WACCM has the fully interactive chemistry described in Mills et al. (2016), and we
146 have included the Na chemistry scheme listed in Plane et al. (2015) and Gomez Martin et al.
147 (2015, 2017), with an updated meteoric input function (MIF) for Na (Cárrillo-Sanchez et
148 al., 2016). The new MIF is calculated for the ablation of cosmic dust particles from Jupiter
149 Family Comets (80% by mass), Asteroids (8%), and Long Period Comets (12%), and the
150 injection rate of Na is about 8 times larger than that used in Marsh et al. (2013). The peak Na
151 ablation rate from Cárrillo-Sanchez et al. (2016) occurs around 87 km, which is ~15 km lower
152 than the MIF used in Marsh et al. (2013), which was based on meteor head radar
153 measurements which were biased to the high velocity dust particles which mostly originate
154 from Long Period Comets (Cárrillo-Sanchez et al., 2016). The absolute Na MIF used in this
155 paper has been divided by a factor of 5 from that in Cárrillo-Sanchez et al. (2016), in order to
156 match the observed Na layer density. This most likely reflects the fact that WACCM
157 underestimates the rate of vertical transport of Na species in the MLT because sub-grid
158 gravity waves are not resolved in the model (Huang et al., 2015). The horizontal resolution of
159 WACCM is 1.9° latitude by 2.5° longitude. The vertical model layers and the vertical
160 resolution are the same as Mills et al. (2017), which is 70 and ~3 km in the MLT region.
161 Although the model can be nudged by a re-analysis dataset, in the current study we have used
162 a “free-running” model [simulation, which](#) produces a satisfactory Na climatology in the
163 model. We ran the model for year 2000 condition for 13 years.

164 The lidar raw photon counts are first analyzed to generate hourly mean vertical profiles
165 of sodium density, temperature and line-of-sight (LOS) wind with 2 km vertical resolution for
166 each direction. Before and after the dual-beam setup (eastward-westward) between December
167 2012 and May 2014, we assume that the hourly mean vertical wind is negligible and then
168 derive the hourly mean zonal wind from the east channel LOS wind (eastward pointing at 30°
169 from zenith). During the dual-beam setup, we derive the hourly mean zonal wind profiles by
170 subtracting the hourly westward LOS wind from the eastward LOS wind and then dividing by
171 $2\sin\theta$ (e.g. $\theta=20^\circ$) (Vincent and Reid, 1983). The uncertainties of the hourly mean zonal wind
172 and temperature typically range from ~1.0 m/s and ~0.5 K at 92 km (Na peak layer) to ~6 m/s

Author

Deleted: simulation which

174 and ~5 K at 82 km and 103 km (the edge of Na layer), respectively. We then generate the
175 nighttime hourly mean composite in each season.

176 Vincent and Reid (1983) presented a method utilizing the dual beam technique to derive
177 vertical flux of GW horizontal momentum, when two beams are pointed at equal and opposite
178 angle θ from the zenith. The zonal momentum flux $\overline{w'u'}$ is calculated as follows:

$$179 \quad \overline{w'u'} = \frac{\overline{v^2(\theta,R)} - \overline{v^2(-\theta,R)}}{2\sin(2\theta)} \quad (1)$$

180 where $\overline{v^2(\theta,R)}$ and $\overline{v^2(-\theta,R)}$ are the square of the LOS wind perturbations in the east and
181 west channels respectively, and θ is the zenith angle (e.g. 20°). To derive the momentum flux,
182 we employed a similar procedure to that of Gardner and Liu (2007). Briefly, we first analyze
183 lidar raw photon counts to generate the LOS wind with a temporal resolution of 5 min and a
184 vertical resolution of 2 km. Data points with errors larger than 5 m/s were discarded during
185 the quality check. We remove the linear trend and nightly mean from the LOS wind to form
186 wind perturbations for each night. Data where the perturbation variances are smaller than the
187 corresponding noise variances are also excluded. The seasonal mean vertical profile of
188 perturbation variance is then obtained by averaging all available perturbation variances in that
189 season. This process is done separately for each beam. Finally, the seasonal mean momentum
190 flux is calculated using equation (1). In this way, the results only account for the GW
191 perturbations with periods of 10 min-20 hr and vertical wavelengths of 4-30 km. [We also
192 apply a high-pass filter with cutoff at 2 hr on raw perturbations to examine the relative
193 contribution of short-period GWs \(10 min - 2 hr\) to total momentum flux.](#)

194 Since the [meteor](#) radar observed zonal wind is only available in 2013, we then calculate
195 monthly mean with all available data for comparison. The SABER tracking points within $\pm 5^\circ$
196 latitude band (27-37°N) and longitude band (112-122°E) of the lidar site are selected first. We
197 then discard the SABER temperature profiles that are outside of the lidar observation period.
198 Finally, we average all available SABER temperature profiles within each month to form the
199 monthly mean for comparison. A similar analysis method is used for the OSIRIS data. In the
200 case of WACCM, the zonal mean data are first extracted at the coordinates of the lidar site
201 and then the monthly mean profiles are generated in the same way as the lidar and radar
202 profiles.

203

Author
Deleted: wnal

Author
Deleted: -

Author
Deleted:

Author
Formatted: Font:(Default) Times New Roman

Author
Formatted: Normal, Indent: First line: 0 cm

207 **3. Temperature and sodium density**

208 Figure 2 shows the hourly mean temperature composite in four different seasons. The
209 temperatures below 95 km are generally warmer in fall and winter than in spring and summer,
210 consistent with the mesospheric residual meridional circulation with upwelling in the summer
211 hemisphere and downwelling in the winter hemisphere (Andrew et al., 1987; Smith, 2012). It
212 is most likely that the diurnal tide with downward phase progression dominates below 100 km
213 in spring, although we only have 10-12 hr data. However, the tidal feature is not clear below
214 95 km in other seasons. The temperature above 100 km in all seasons clearly exhibits two
215 minima after dusk and before dawn and a maximum near midnight, suggesting dominance
216 and persistence of the semidiurnal tide in this latitude region throughout the year.

217 The clear downward phase progression of diurnal and semidiurnal tides in mesopause
218 temperature was previously observed by sodium lidar at the Starfire Optical Range (SOR),
219 New Mexico (35°N, 107°W) (Chu et al., 2005). However, their observations suggest a clear
220 dominance of diurnal in April and October and semidiurnal in January below 100 km, while
221 we see a clear dominance of diurnal only in spring (March-May), and mixed features in other
222 seasons. In addition, the midnight maximum above 100 km shown in our results is not
223 observed over SOR. [The SABER observations reveal a diurnal amplitude of ~2 K and ~8 K,
224 and semidiurnal amplitude of ~7 K and ~12 K at 95km for the USTC and SOR lidar sites,
225 respectively \(Zhang et al., 2010\). This significant longitudinal variability is likely due to
226 nonlinear interactions between the migrating tide and non-immigrating tide \(Forbes et al.,
227 2003\) and stationary planetary wave number 1 \(Lieberman et al., 1991\), respectively, and/or
228 tidal/gravity waves interactions \(Lindzen, 1981; Liu and Hagan, 1998; Li et al., 2007; 2009\).
229 The clear longitudinal variability of tides between two lidar sites could thus cause significant
230 differences in the nocturnal climatology.](#)

231 Figure 3 shows the monthly mean of the nightly mean temperature observed by lidar and
232 SABER, and simulated by WACCM. All three figures show qualitative agreement in the
233 general pattern, but difference in absolute values. The mesopause is clearly located near 100
234 km in winter and below 95 km in summer, indicating a two-level mesopause as previously
235 observed at mid- and high latitudes (von Zahn et al., 1996; She et al., 1998). The lidar
236 observed temperature above 95 km is ~10 K lower than SABER, likely due either to the low
237 signal-to-noise ratio in the lidar return signals above 100 km (Li et al., 2012), or to a non-local

Author
Formatted ... [1]

Author
Deleted: the

Author
Formatted ... [2]

Author
Formatted ... [3]

Author
Formatted ... [4]

Author
Formatted ... [5]

Author
Formatted ... [6]

Author
Formatted ... [7]

Author
Formatted ... [8]

Author
Formatted ... [9]

Author
Formatted ... [10]

Author
Formatted ... [11]

Author
Deleted: could be

Author
Formatted ... [12]

Author
Formatted ... [13]

Author
Formatted ... [14]

Author
Formatted ... [15]

Author
Formatted ... [16]

Author
Deleted: Currently, we do not have ... [17]

Author
Deleted: and their

Author
Deleted: with the tides

Author
Formatted ... [18]

Author
Formatted ... [19]

Author
Formatted ... [20]

Author
Formatted ... [21]

Author
Deleted: of

Author
Formatted ... [22]

247 thermal equilibrium influence in the SABER analysis (Mertens et al., 2001). The lidar
248 observed mesopause is also 5-10 K colder than that observed by SABER. The WACCM
249 simulated temperature is clearly higher than both sets of observations at most altitudes and
250 months. Yuan et al. (2008) showed a significant monthly mean mesopause region temperature
251 difference between lidar observations and WACCM simulations over Fort Collins, CO (41°N,
252 105°W); their comparisons show that the WACCM-simulated winter mesopause is much
253 warmer than measured by lidar, and the summer mesopause is ~3 km lower than lidar
254 observations. Another interesting feature in all three figures is that we see a temperature
255 maximum near ~90 km in March and April, and a second maximum in September and
256 October, likely related to the mesospheric semiannual oscillation (MSAO) usually dominant
257 in the equatorial middle atmosphere (Dunkerton, 1982; Burrage et al., 1996; Garcia et al.,
258 1997).

259 Our measured monthly means of the nightly mean temperatures are also generally
260 consistent with previously lidar observations at SOR (Gardner and Liu, 2007) and Fort
261 Collins, CO (She et al., 1998; Yuan et al., 2008). However, the SOR lidar observations were
262 ~10 K colder below 90 km in summer, and ~10 K warmer between 90 and 95 km in spring,
263 suggesting significant differences between the two locations [likely induced by the significant](#)
264 [longitudinal variability of the diurnal tide \(Zhang et al., 2010\)](#). The semiannual oscillation
265 signature is evident over both Hefei and SOR between 90 and 95 km, but not over Fort
266 Collins. The summer mesopause observed by lidar over Hefei is clearly higher than over the
267 other two locations.

268 Figure 4 shows the hourly mean sodium density composite during the four different
269 seasons. The density increases with local time during the night, with a peak height around 92
270 km. The peak density is overall much higher in fall and winter than in spring and summer,
271 which is consistent with previous ground-based and satellite observations (She et al., 2000;
272 Fan et al., 2007a; Fussen et al., 2010). Some peaks above 95 km in summer are likely induced
273 by sporadic sodium layers (SSLs), which often occur in this season over Hefei (Dou et al.,
274 2010). The seasonal mean sodium peak density in winter can reach 4000-4500 cm⁻³ after
275 midnight. Figure 5 shows the monthly mean of nightly mean sodium density observed by (a)
276 lidar and (b) Odin/OSIRIS, and simulated by (c) WACCM. Both observations agree well in
277 seasonal pattern and absolute sodium density, and are also consistent with the WACCM

278 model simulation. The elevated peak height and enhanced density in summer observed by
279 lidar is likely due to increased SSL events in summer over Hefei, which is neither frequently
280 observed by Odin/OSIRIS nor simulated by WACCM. The Odin/OSIRIS did observe SSLs
281 over China (Fan et al., 2007b), but probably less frequently at 0600 and 1800 local time than
282 at midnight. The observed sodium density over Hefei is quite consistent with previous
283 narrowband lidar observations over Fort Collins, CO (She et al., 2000) and Urbana, IL (States
284 and Gardner, 1998), but ~1.5 times higher than previous broadband sodium lidar observations
285 over the nearby city of Wuhan, China (Yi et al., 2009).

286 The variability of sodium density is clearly correlated with the temperature variability
287 shown in Figure 2. This is further demonstrated in Figure 6, where the correlation coefficient
288 between the composite temperature and relative sodium density perturbations is plotted using
289 lidar measurements (left) and the WACCM simulation (right). The temporal resolution for
290 both lidar and WACCM is 1 hr. We also examined the correlation in the four different
291 seasons and found no significant differences. The lidar observations are clearly consistent
292 with the WACCM simulation, and both results suggest a positive correlation with coefficient
293 of 0.5-0.8 between 80-90 km, but a negative correlation with coefficient of less than ~-0.4
294 above 96 km for lidar and 100 km for WACCM, consistent with lidar observations at Urbana
295 (40N) (Plane et al., 1999) and in the Arctic (Collins and Smith, 2004). However, our lidar
296 observations above 95 km are not consistent with the recent sodium lidar observations at
297 ALOMAR, which showed a positive correlation with temperature above this altitude (Dunker
298 et al., 2015). This difference may be related to energetic particle precipitation at high latitudes,
299 but the detailed mechanism is beyond scope of this paper.

300 Our lidar observations suggest that the main chemistry below 95 km is likely dominated
301 by neutral sodium chemistry, which essentially involves the partitioning of the metal between
302 atoms and the main reservoir NaHCO_3 ; the significant activation energy of the reaction
303 $\text{NaHCO}_3 + \text{H}$ drives the balance towards Na at higher temperatures. In contrast, above 95 km
304 the source of atomic Na is from Na^+ , which involves formation of cluster ions that then
305 undergo dissociative recombination with electrons; the formation of cluster ions is favored at
306 lower temperatures, hence the negative correlation coefficient between and Na and
307 temperature on the topside of the Na layer (Plane et al., 2015).

308

Author
Formatted: Font:(Default) Times New Roman, 12 pt

Author
Formatted: Font:(Default) Times New Roman, 12 pt

Author
Deleted: 4

Author
Formatted: Font:(Default) Times New Roman, 12 pt

Author
Deleted: much

Author
Formatted: Font:(Default) Times New Roman, 12 pt

Author
Deleted: i

Author
Formatted: Font:(Default) Times New Roman, 12 pt

Author
Formatted: Font:(Default) Times New Roman, 12 pt

Author
Comment [1]: Plane, J.M.C., C.S. Gardner, J. Yu, C.Y. She, R.R. Garcia and H.C. Pumphrey (1999), The Mesospheric Na layer at 40°N: Modelling and Observations. *Journal of Geophysical Research*, 104, 3773-3788

Author
Deleted: early model simulation in the high latitude

Author
Deleted: It should be noted that

315 **4. Zonal wind and gravity wave momentum flux**

316 Figure 7 shows the hourly mean zonal wind composite in 4 different seasons. We see
317 strong tidal oscillations with downward phase progression in all seasons, much clearer than
318 those in temperature (Figure 2). The diurnal tide with vertical wavelength of ~ 20 km
319 dominates in both spring and fall, while the semidiurnal tide with vertical wavelength of
320 30-40 km dominates in winter. In spring, the diurnal tide in temperature (Figure 2a) leads that
321 in zonal wind by ~ 4 hr between 90 and 95 km, consistent with earlier mid-latitude
322 observations (Yuan et al., 2006). There is a strong wave oscillation signature with a period of
323 ~ 8 hr and amplitude of ~ 20 m/s that dominates in summer, possibly related to the terdiurnal
324 tide. Previous observations by the nearby Wuhan meteor radar show that the diurnal
325 amplitude near 90 km during equinox is ~ 30 m/s, with a semidiurnal amplitude of ~ 10 m/s
326 (Xiong et al., 2004; Zhao et al., 2005). The comparable amplitude (~ 10 m/s) of diurnal and
327 semidiurnal in winter is also revealed by these radar observations, with which our
328 observations are generally consistent.

329 We show in Figure 8 the monthly mean of the nightly mean zonal wind observed by (a)
330 lidar, (b) Wuhan meteor radar, and (c) simulated by WACCM. The radar observed zonal wind
331 is only available in 2013 for comparison. The general pattern of the lidar observed zonal
332 winds agrees well with the radar winds, but are 5-10 m/s stronger. This is likely due to the
333 different vertical and temporal resolutions, [signal-to-noise ratio](#), and the measurement methods,
334 as well as the different locations. The lidar results exhibit a semiannual variation near 90 km
335 with minima in March and August/September, and one maximum in May/June, clearly
336 out-of-phase with the temperature semiannual variation (Figure 3a). The lidar observed
337 semiannual variation in both wind and temperature is consistent with the tropical MSAO
338 previously observed by satellites (Garcia et al., 1997), and simulated by WACCM (Richter
339 and Garcia, 2006). [The lidar and radar observations agree with the WACCM simulation
340 below 90 km in both pattern and magnitude, while disagreeing above.](#) Interestingly, a recent
341 comparison between lidar measurements over Fort Collins, CO and several general
342 circulation models also reveals significant differences (Yuan et al., 2008).

343 The USTC lidar telescopes were pointed 15° from zenith in eastward and westward
344 directions between December 2012 and May 2014. This setup allows us to derive the vertical
345 flux of GW zonal momentum. A total of 83 nights of GW momentum flux measurements

Author
Deleted:

Author
Deleted: Wuhan meteor

Author
Deleted: possibly

Author
Deleted: Both observations agree with the WACCM simulation below 90 km in both pattern and magnitude, while disagreeing above.

Author
Deleted: 20

354 were obtained with 21, 12, 23, and 27 nights in spring, summer, fall, and winter respectively.

355 Figure 9 shows vertical profiles of the seasonal mean GW zonal momentum flux for period

356 10min – 16hr (blue) and 10min – 2hr (green), and zonal wind (red) in (a) spring, (b) summer,

357 (c) fall, and (d) winter. The zonal momentum flux is mostly eastward in spring, positively

358 correlated with the eastward zonal wind. However, the zonal momentum flux is mostly

359 westward in other seasons, clearly anti-correlated with the eastward zonal wind, suggesting

360 zonal wind filtering of GWs below 80 km. It is also clear that the zonal momentum flux

361 induced by short-period (10 min – 2 hr) GWs clearly dominates total momentum flux in all

362 seasons except summer.

363 The seasonal variation of zonal momentum flux is consistent with previous sodium lidar

364 observation at SOR, NM (Gardner and Liu, 2007). However, MU radar observations near

365 Kyoto, Japan (35°N, 136°E) shows a clear eastward flux in summer and westward flux in

366 winter between 65 and 85 km (Tsuda et al., 1990). MF radar observations in Adelaide,

367 Australia (35°S, 138°E) suggest an eastward flux of ~3 m²/s² in winter (Reid and Vincent,

368 1987). We note here that part of the differences between our lidar results and other published

369 work is likely due to different vertical and temporal resolutions and thus sensitivity to

370 different portions of the GW spectrum. Table 1 compares the GW zonal momentum flux

371 measured at different mid-latitude lidar and radar stations. The results from other locations are

372 estimated from the following studies: Gardner and Liu (2007) for the SOR lidar results; Acott

373 et al. (2009) for the Fort Collins, CO lidar results; and Tsuda et al. (1990) for the Japan MU

374 radar results. This comparison demonstrates that all observations report a clear westward GW

375 zonal momentum flux in winter. In spring, both the USTC and SOR lidars observed an

376 eastward momentum flux of 1.4–2 m²/s².

377 The short-period (10 min – 2 hr) GWs clearly contribute 50%-70% of the total

378 momentum flux, consistent with previously medium frequency (MF) radar observations

379 (Fritts and Vincent, 1987). The large westward momentum fluxes of -0.9 and -0.6 m²/s² for

380 short-period GWs in summer and winter respectively are clearly anti-correlated with eastward

381 zonal wind maxima below 90 km (Figure 8a), suggesting the filtering of short-period GWs by

382 the SAO wind. However, this SAO variation is not clear in the total momentum flux. For the

383 annual mean, our lidar result is clearly smaller than the SOR lidar result, mainly due to

384 significant difference in summer. Our results also show that the annual mean zonal wind

Author
Deleted: of nightly mean

Author
Deleted: both fall and winter

Author
Deleted: In summer, the zonal momentum flux is small and variable with altitude, likely due to much less data in this season.

Author
Deleted: is

Author
Formatted: Font:(Default) Times New Roman, 12 pt

Author
Deleted: °

Author
Deleted: °

Author
Deleted: The

Author
Formatted: Font:(Default) Times New Roman, 12 pt

Author
Formatted: Font:(Default) Times New Roman, 12 pt

Author
Formatted: Font:(Default) Times New Roman, 12 pt

Author
Formatted: Superscript

Author
Formatted: Superscript

Author
Deleted:

Author
Deleted: with other results

Author
Deleted: e

Author
Deleted: .

Author
Deleted: 5

Author
Deleted: the byon the

400 averaged between 87-95 km is ~ 10 m/s eastward, and anti-correlated with the westward
401 momentum flux of $\sim 0.15 \text{ m}^2/\text{s}^2$ induced by short-period GWs. This anti-correlation suggests
402 that the GW momentum flux observed in the mesopause region is generally consistent with
403 the wind filtering theory, proposed by Lindzen (1981), and adopted by general circulation
404 models (e.g. Richter et al., 2010).

405

406 5. Summary

407 Between 2012 and 2016, the USTC sodium temperature/wind lidar observed mesopause
408 region nighttime temperature, zonal wind, and sodium density over 150 nights, and the
409 vertical flux of zonal momentum during 83 nights. The seasonal nighttime hourly composites
410 of temperature and zonal wind show clear diurnal and/or semidiurnal tidal signatures. In
411 temperature, the diurnal tide with clear downward phase progression dominates only in spring,
412 while the semidiurnal tide dominates above 100 km throughout the year. In zonal wind, the
413 diurnal tide with vertical wavelength of ~ 20 km dominates in both spring and fall, while the
414 semidiurnal tide with vertical wavelength of 30-40 km dominates in winter. Between 90 and
415 95 km, the diurnal tide in temperature in spring leads that in zonal wind by ~ 4 hr, consistent
416 with previous observations and model simulations. The monthly mean results show a
417 signature of semiannual variation in both temperature and zonal wind near 90 km but with
418 clear out-of-phase feature, consistent with the tropical MSAO. Comparison of the USTC lidar
419 results with observations by satellite and meteor radar, and simulated by WACCM show
420 generally good agreement, although there are some differences among them, with pronounced
421 disagreement between the observed zonal wind and the model above 90 km.

422 The seasonal mean of zonal momentum flux is mostly westward in summer, fall and
423 winter, clearly anti-correlated with the eastward zonal wind, which suggests zonal wind
424 filtering of GWs below 80 km. However, during spring the zonal momentum flux is mostly
425 eastward, positively correlated with the eastward zonal wind. The short-period GWs clearly
426 contribute 50%-70% of total momentum flux averaged over 87-95 km. The large westward
427 momentum fluxes in summer and winter for short-period GWs are clearly anti-correlated with
428 eastward zonal wind maxima below 90 km (Figure 8a), suggesting the filtering of
429 short-period GWs by the SAO wind. The annual mean flux averaged over 87-95 km is ~ 0.15
430 m^2/s^2 (westward) induced by the short-period GWs, anti-correlated with the zonal wind of

Author
Deleted: 7
Author
Deleted: 3
Author
Deleted: the
Author
Deleted: (especially in winter)

Author
Deleted: Hefei
Author
Deleted: between
Author
Deleted: of the nightly mean vertical flux of
Author
Deleted: both
Author
Formatted: Indent: First line: 0.74 cm
Author
Deleted: by
Author
Deleted: In summer, the flux is small over the whole altitude range.
Author
Deleted: 7
Author
Deleted: 3

444 ~10 m/s (eastward), suggesting that the GW momentum flux observed in the mesopause
445 region is generally consistent with the wind filtering theory. ▾

446 The sodium density increases with local time during the night, with a peak height near 92
447 km. The peak density is overall much higher in fall and winter than in spring and summer.
448 The seasonal mean sodium peak density in winter can reach 4000-4500 cm⁻³ after mid-night.
449 The variability of sodium density is positively correlated with temperature variability,
450 suggesting that chemistry plays a dominant role in the formation of sodium atoms in the
451 mesopause region below 95 km. The lidar observations agree well with Odin/OSRIS satellite
452 observations in both seasonal pattern and absolute monthly mean sodium density, consistent
453 with WACCM simulations using a new Na meteoric input function.

454

455 Acknowledgments

456 The work described in this paper was carried out at the University of Science and
457 Technology of China (USTC), under support of the National Natural Science Foundation of
458 China grant [41674149](#) and [the Open Research Project of Large Research Infrastructures of](#)
459 [CAS - "Study on the interaction between low/mid-latitude atmosphere and ionosphere based](#)
460 [on the Chinese Meridian Project.](#) WF and JMCP were supported by the European Research
461 Council (project 291332-CODITA). The National Center for Atmospheric Research (NCAR)
462 is sponsored by the National Science Foundation. We thank Chengyun Yang, Shengyang Gu,
463 Xianyu Wang, Yetao Cen, Feng Li, and Huazhi Ge for help to take lidar data. TL would like
464 to thank Alan Liu for helpful discussion. The SD-WACCM model was obtained from the
465 NCAR and run at the University of Leeds and is available for contacting the co-authors FW or
466 JMCP. We would like to thank Francis Vitt at NCAR for the WACCM model support. The
467 SABER data is downloaded from <http://saber.gats-inc.com/>. [We thank Richard Collins and](#)
468 [another anonymous reviewer for their constructive comments.](#)

Author

Deleted: This is especially clear in winter with a westward flux of -1.2 m²/s² corresponding to an eastward zonal wind of ~-10 m/s.

Author

Deleted: s

Author

Deleted: (

Author

Formatted: Font:Times New Roman, 12 pt, Not Bold

Author

Deleted: , 41225017).

476 **Reference:**

477 Acott, P. E., C. Y. She, D. A. Krueger, Z. A. Yan, T. Yuan, J. Yue, and S. Harrell (2011),
478 Observed nocturnal gravity wave variances and zonal momentum flux in mid-latitude
479 mesopause region over Fort Collins, Colorado, USA, *J. Atmos. Sol. Terr. Phys.*, 73(4),
480 449–456, doi:10.1016/j.jastp.2010.10.016.

481 Andrews, D. G., J. R. Holton, and C. B. Leovy (1987), *Middle Atmosphere Dynamics*, 489
482 pp., Elsevier, New York.

483 Arnold, K., and C. She (2003), Metal fluorescence lidar (light detection and ranging) and the
484 middle atmosphere, *Contemporary Physics*, 44(1), 35–49,
485 doi:10.1080/0010751021000019157.

486 Burrage, M. D., R. A. Vincent, H. G. Mayr, W. R. Skinner, N. F. Arnold, and P. B. Hays
487 (1996), Long-term variability in the equatorial middle atmosphere zonal wind, *J.*
488 *Geophys. Res.*, 101(D), 12–, doi:10.1029/96JD00575.

489 Carrillo-Sánchez, J. D., D. Nesvorný, P. Pokorný, D. Janches, and J. M. C. Plane (2016),
490 Sources of cosmic dust in the Earth's atmosphere, *Geophys. Res. Lett.*, 43, 11,979–
491 11,986, doi:10.1002/2016GL071697.

492 Chu, X., C. S. Gardner, and S. J. Franke (2005), Nocturnal thermal structure of the
493 mesosphere and lower thermosphere region at Maui, Hawaii (20.7°N), and Starfire
494 Optical Range, New Mexico (35°N), *J. Geophys. Res.*, 110(D), D09S03,
495 doi:10.1029/2004JD004891.

496 [Collins, R. L. and Smith, R. W.: Evidence of damping and overturning of gravity waves in the](#)
497 [Arctic mesosphere: Na lidar and OH temperature observations, *J. Atmos. Sol. Terr. Phys.*,](#)
498 [66\(10\), 867–879, doi:10.1016/j.jastp.2004.01.038, 2004.](#)

499 Dou, X., - K., X., - H. Xue, T. Li, T., - D. Chen, C. Chen, and S., - C. Qiu (2010), Possible
500 relations between meteors, enhanced electron density layers, and sporadic sodium layers,
501 *J. Geophys. Res.*, 115, A06311, doi:10.1029/2009JA014575.

502 Dawkins, E. C. M., J. M. C. Plane, M. P. Chipperfield, W. Feng, J. Gumbel, J. Hedin, J.
503 Hoffner, and J. S. Friedman (2014): First global observations of the mesospheric
504 potassium layer, *Geophys. Res. Lett.*, 41, 5653-5661.

505 Dunker, T., U.-P. Hoppe, W. Feng, J. M. C. Plane, and D. R. Marsh (2015), Mesospheric
506 temperatures and sodium properties measured with the ALOMAR Na lidar compared

Author
Formatted: Font:(Default) Times New Roman

Author
Formatted: Font:(Default) Times New Roman

Author
Formatted: Font:(Default) Adobe Caslon Pro Bold

Author
Formatted: Font:(Default) Adobe Caslon Pro Bold

Author
Formatted: Font:(Default) Adobe Caslon Pro Bold

Author
Formatted: Font:(Default) Adobe Caslon Pro Bold

507 | with WACCM, [J. Atmos. Sol. Terr. Phys.](#), 127, 111–119,
508 | doi:10.1016/j.jastp.2015.01.003.

509 | Dunkerton, T. J. (1982), Theory of the Mesopause Semiannual Oscillation, *J. Atmos. Sci.*,
510 | 39(12), 2681–2690, doi:10.1175/1520-0469(1982)039<2681:TOTMSO>2.0.CO;2.

511 | Ejiri, M. K., T. Nakamura, and T. D. Kawahara (2010), Seasonal variation of nocturnal
512 | temperature and sodium density in the mesopause region observed by a resonance scatter
513 | lidar over Uji, Japan, *J. Geophys. Res.*, 115, D18126, doi:10.1029/2009JD013799.

514 | Espy, P. J., G. O. L. Jones, G. R. Swenson, J. Tang, and M. J. Taylor (2004), Seasonal
515 | variations of the gravity wave momentum flux in the Antarctic mesosphere and lower
516 | thermosphere, *J. Geophys. Res.*, 109, D23109, doi:10.1029/2003JD004446.

517 | Fan, Z. Y., J. M. C. Plane, J. Gumbel, J. Stegman, and E. J. Llewellyn (2007a), Satellite
518 | measurements of the global mesospheric sodium layer, *Atmospheric Chemistry and*
519 | *Physics*, 7, 4107–4115.

520 | Fan, Z. Y., J. M. C. Plane, and J. Gumbel (2007b), On the global distribution of sporadic
521 | sodium layers, *Geophysical Research Letters*, 34, Article number L15808

522 | Feng, W., Marsh, D. R., Chipperfield, M. P., Janches, D., Hoffner, J. Yi, F., and Plane, J. M.
523 | C. (2013): A global atmospheric model of meteoric iron, *Journal of Geophysical*
524 | *Research*, 118, 9456–9474.

525 | Feng, W., B. Kaifler, D. R. Marsh, J. Höffner, U.-P. Hoppe, B. P. Williams, and J. M. C.
526 | Plane (2017), Impacts of a sudden stratospheric warming on the mesospheric metal layers,
527 | *J. Atmos. Sol. Terr. Phys.*, 1–10, doi:10.1016/j.jastp.2017.02.004.

528 | [Forbes, J. M., X. Zhang, W. Ward, and E. Talaat \(2003\), Nonmigrating diurnal tides in the](#)
529 | [thermosphere, *J. Geophys. Res.*, 108\(A1\), 1033, doi:10.1029/2002JA009262.](#)

530 | Franke, S. J., X. Chu, A. Z. Liu, and W. K. Hocking (2005), Comparison of meteor radar and
531 | Na Doppler lidar measurements of winds in the mesopause region above Maui, Hawaii, *J.*
532 | *Geophys. Res.*, 110, D09S02, doi:10.1029/2003JD004486.

533 | Friedman, J. S., S. C. Collins, R. Delgado, and P. A. Castleberg (2002), Mesospheric
534 | potassium layer over the Arecibo Observatory, 18.3°N 66.75°W, *Geophys. Res. Lett.*,
535 | 29(5), 1071, doi:10.1029/2001GL013542.

536 | Friedman, J.S., Chu,X. (2007) Nocturnal temperature structure in the mesopause region over
537 | the Arecibo Observatory (18.351N, 66.751W): seasonal variations. *J. Geophys. Res.*,

Author

Deleted: Journal of Atmospheric and
Solar-Terrestrial Physics

Author

Formatted: Font:(Default) Times New
Roman, 12 pt

Author

Formatted

540 112(D11), D14107.

541 [Fritts, D. and Vincent, R.: Mesospheric Momentum Flux Studies at Adelaide, Australia:
542 \[Observations and a Gravity Wave-Tidal Interaction Model, Journal of the Atmospheric
543 \\[Sciences, 44\\\(3\\\), 605–619, 1987.\\]\\(#\\)\]\(#\)](#)

544 Fussen, D., Vanhellemont, F., Tétard, C., Matshvili, N., Dekemper, E., Loodts, N., et al.
545 (2010). A global climatology of the mesospheric sodium layer from GOMOS data during
546 the 2002-2008 period. *Atmospheric Chemistry and Physics*, 10(1), 9225–9236,
547 doi:10.5194/acp-10-9225-2010.

548 Garcia, R. R., T. J. Dunkerton, R. S. Lieberman, and R. A. Vincent (1997), Climatology of
549 the semiannual oscillation of the tropical middle atmosphere, *J. Geophys. Res.*, 102(D),
550 26–, doi:10.1029/97JD00207.

551 Garcia, R. R., D. Marsh, D. E. Kinnison, B. Boville, and F. Sassi, Simulations of secular
552 trends in the middle atmosphere, 1950-2003, *J. Geophys. Res.*, 112, D09301,
553 doi:10.1029/2006JD007485, 2007.

554 Gardner, C. S., Y. Zhao, and A. Z. Liu (2002), Atmospheric stability and gravity wave
555 dissipation in the mesopause region, *J. Atmos. Sol. Terr. Phys.*, 64, 923– 929,
556 doi:10.1016/S1364-6826(1002)00047-00040.

557 Gardner, C. S., J. M. C. Plane, W. Pan, T. Vondra, B. J. Murray, and X. Chu (2005), Seasonal
558 variations of the Na and Fe layers at the South Pole and their implications for the
559 chemistry and general circulation of the polar mesosphere, *J. Geophys. Res.*, 110,
560 D10302, doi:10.1029/2004JD005670.

561 Gardner, C. S., and Liu A. Z. (2007), Seasonal variations of the vertical fluxes of heat and
562 horizontal momentum in the mesopause region at Starfire Optical Range, New Mexico, *J.*
563 *Geophys. Res.*, 112, D09113, doi:10.1029/2005JD006179.

564 Gómez Martín, J.C., et al., Reaction Kinetics of Meteoric Sodium Reservoirs in the Upper
565 Atmosphere, *J. Phys. Chem. A*, 2015, DOI: 10.1021/acs.jpca.5b00622

566 Gómez Martín, J.C., et al., The Reaction Between Sodium Hydroxide and Atomic Hydrogen
567 in Atmospheric and Flame Chemistry, *J. Phys. Chem. A*, 2017,
568 doi:10.1021/acs.jpca.7b07808.

569 Huang, W.; Chu, X. Z.; Gardner, C. S.; Carrillo-Sanchez, J. D.; Feng, W.; Plane, J. M. C.;
570 Nesvorny, D. (2015): Measurements of the vertical fluxes of atomic Fe and Na at the

Author

Formatted: Font:(Default) Times New Roman

Author

Formatted: Font:(Default) Times New Roman

571 mesopause: Implications for the velocity of cosmic dust entering the atmosphere,
572 *Geophysical Research Letters*, 42, 169-175.

573 Hurrell, J. W., Holland, M. M., Gent, P. R., Ghan, S., Kay, J. E., Kushner, P. J., Lamarque, J.
574 F., Large, W. G., Lawrence, D., Lindsay, K., Lipscomb, W. H., Long, M. C., Mahowald,
575 N., Marsh, D. R., Neale, R. B., Rasch, P., Vavrus, S., Vertenstein, M., Bader, D., Collins,
576 W. D., Hack, J. J., Kiehl, J. and Marshall, S.: The Community Earth System Model: A
577 Framework for Collaborative Research, *Bulletin of the American Meteorological Society*,
578 94(9), 1339–1360, doi:10.1175/BAMS-D-12-00121.1, 2013.

579 Kudeki, E., and S. J. Franke (1998), Statistics of momentum flux estimation, *J. Atmos. Sol.*
580 *Terr. Phys.*, 60, 1549– 1553.

581 Lauritzen, P. H., Bacmeister, J. T., Callaghan, P. F., and Taylor, M. A.: NCAR global model
582 topography generation software for unstructured grids, *Geosci. Model Dev.*, 8, 1-12,
583 doi:10.5194/gmd-8-1-2015, 2015

584 Li, T., C. She, B. Williams, T. Yuan, R. Collins, L. Kieffaber, and A. Peterson (2005),
585 Concurrent OH imager and sodium temperature/wind lidar observation of localized
586 ripples over northern Colorado, *J. Geophys. Res.*, 114, D06106,
587 doi:10.1029/2008JD011089.

588 Li, T., C. She, H. Liu, and M. Montgomery (2007), Evidence of a gravity wave breaking
589 event and the estimation of the wave characteristics from sodium lidar observation over
590 Fort Collins, CO (41°N, 105°W), *Geophys. Res. Lett.*, 34, L05815,
591 doi:10.1029/2006GL028988.

592 Li, T., C.-Y. She, H.-L. Liu, J. Yue, T. Nakamura, D. A. Krueger, Q. Wu, X. Dou, and S.
593 Wang (2009), Observation of local tidal variability and instability, along with dissipation
594 of diurnal tidal harmonics in the mesopause region over Fort Collins, Colorado (41°N,
595 105°W), *J. Geophys. Res.*, 114, D06106, doi:10.1029/2008JD011089.

596 Li, T., X. Fang, W. Liu, S. Y. Gu, and X. K. Dou (2012), Narrowband sodium lidar for the
597 measurements of mesopause region temperature and wind, *Appl. Optics*, 51(22),
598 5401-5411, doi:10.1364/ao.51.005401.

599 Li, T., N. Calvo, J. Yue, X. Dou, J. M. Russell III, M. G. Mlynczak, C.-Y. She, and X. Xue
600 (2013), Influence of El Niño-Southern Oscillation in the mesosphere, *Geophys. Res. Lett.*,
601 40(12), 3292–3296, doi:10.1002/grl.50598.

602 | Li, T., N. Clavo, J. Yue, J. Russel III, A. Smith, M. Mlynczak, A. Chandran, X. Dou, and A.
603 | Liu (2016), Southern Hemisphere summer mesopause responses to El Niño–Southern
604 | Oscillation, *J. Clim.*, 29, 6319–6328, doi:10.1175/JCLI-D-15-0816.1.
605 | [Lieberman, R. S. \(1991\), Nonmigrating diurnal tides in the equatorial middle atmosphere, *J.*
606 | \[Atmos. Sci.\]\(#\), 48, 1112–1123.](#)
607 | Lin, S.–J., A “vertically-Lagrangian” finite-volume dynamical core for global atmospheric
608 | models, *Mon. Wea. Rev.*, 132, 2293-2307, 2004.
609 | Lindzen, R. S. (1981), Turbulence and stress owing to gravity-wave and tidal breakdown, *J.*
610 | *Geophys. Res.*, 86(NC10), 9707-9714, doi:10.1029/JC086iC10p09707.
611 | Liu, H. L., and M. E. Hagan (1998), Local heating/cooling of the mesosphere due to gravity
612 | wave and tidal coupling, *Geophys. Res. Lett.*, 25(15), 2941-2944,
613 | doi:10.1029/98gl02153.
614 | Lübken F, Höffner J, Viehl TP, Kaifler B, Morris RJ (2011), First measurements of thermal
615 | tides in the summer mesopause region at Antarctic latitudes. *Geophys. Res. Lett.*, 38,
616 | L24806. doi:10.1029/2011GL0500458.
617 | Llewellyn, E. J., et al. (2004). The OSIRIS instrument on the Odin spacecraft, *Can. J. Phys.*,
618 | 82, 411–422.
619 | Marsh, D. R., M. J. Mills, D. E. Kinnison, J.-F. Lamarque, N. Calvo, and L. M. Polvani
620 | (2013a), Climate Change from 1850 to 2005 Simulated in CESM1(WACCM), *Journal of*
621 | *Climate*, 26(19), 7372–7391, doi:10.1175/JCLI-D-12-00558.1.
622 | Marsh, D. R., Janches, D., Feng, W., and Plane, J. M. C. (2013b). A global model of meteoric
623 | sodium. *J. Geophys. Res.*, 118(1), 11,442–11,452, doi:10.1002/jgrd.50870.
624 | Mertens, C. J., M. G. Mlynczak, M. López-Puertas, P. P. Wintersteiner, R. H. Picard, J. R.
625 | Winick, L. L. Gordley, and J. M. I. Russell (2001), Retrieval of mesospheric and lower
626 | thermospheric kinetic temperature from measurements of CO₂ 15 μm Earth Limb
627 | Emission under non-LTE conditions, *Geophys. Res. Lett.*, 28(7), 1391–1394,
628 | doi:10.1029/2000GL012189.
629 | Mills, M. J. et al. (2016), Global volcanic aerosol properties derived from emissions,
630 | 1990-2014, using CESM1(WACCM), *J Geophys Res-Atmos*, 121(5), 2332–2348,
631 | doi:10.1002/2015jd024290.
632 | Mills, M. J., Richter, J. H., Tilmes, S., Kravitz, B., MacMartin, D. G., Glanville, A. A.,

Author

Formatted: EndNote Bibliography,
Justified, Indent: Left: 0 cm, Hanging:
4.26 ch, Space After: 0 pt, Line spacing:
1.5 lines, Adjust space between Latin and
Asian text, Adjust space between Asian
text and numbers

Author

Formatted: Font:(Default) Times New
Roman, 12 pt

633 Tribbia, J. J., Lamarque, J.-F., Vitt, F., Schmidt, A., Gettelman, A., Hannay, C.,
 634 Bacmeister, J. T. and Kinnison, D. E.: Radiative and Chemical Response to Interactive
 635 Stratospheric Sulfate Aerosols in Fully Coupled CESM1(WACCM), *Journal of*
 636 *Geophysical Research-Atmospheres*, 6(3), 541, doi:10.1002/2017JD027006, 2017.

637 Neale, R.B., C.C. Chen, A. Gettelman and Coauthors, 2012: Description of the NCAR
 638 Community Atmosphere Model (CAM 5.0). NCAR Tech. Note NCAR-TN-486+STR,
 639 274 pp.

640 [Plane, J. M. C., C. S. Gardner, J. Yu, C.Y. She, R. R. Garcia and H. C. Pumphrey \(1999\), The](#)
 641 [Mesospheric Na layer at 40°N: Modelling and Observations. *Journal of Geophysical*](#)
 642 [Research, 104, 3773-3788.](#)

643 Plane, J. M. C., W. Feng, and E. C. M. Dawkins (2015), The Mesosphere and Metals:
 644 Chemistry and Changes, *Chem. Rev.*, 115(10), 4497–4541, doi:10.1021/cr500501m.

645 Preusse, P., S. D. Eckermann, M. Ern, J. Oberheide, R. H. Picard, R. G. Roble, M. Riese, J. M.
 646 Russell, and M. G. Mlynczak (2009), Global ray tracing simulations of the SABER
 647 gravity wave climatology, *J. Geophys. Res.*, 114(D), D08126,
 648 doi:10.1029/2008JD011214.

649 [Reid, I. M.: Measurements of mesospheric gravity wave momentum fluxes and mean flow](#)
 650 [accelerations at Adelaide, Australia, *Jourmd of Atmospheric and Terresfrial Physrcs*, 1–](#)
 651 [18, 1987.](#)

652 Richter, J. H., F. Sassi, and R. R. Garcia (2010), Toward a Physically Based Gravity Wave
 653 Source Parameterization in a General Circulation Model, *Journal of the Atmospheric*
 654 *Sciences*, 67, 136, doi:10.1175/2009JAS3112.1.

655 Russell, J. M., III, M. G. Mlynczak, L. L. Gordley, J. Tansock, and R. Esplin (1999), An
 656 overview of the SABER experiment and preliminary calibration results, *Proc. SPIE*, 3756,
 657 277– 288.

658 She, C. Y., and J. R. Yu (1994), Simultaneous three-frequency Na lidar measurements of
 659 radial wind and temperature in the mesopause region, *Geophys. Res. Lett.*, 21(1), 1771–
 660 1774, doi:10.1029/94GL01417.

661 She, C.Y., S. W. Thiel, D. A. Krueger (1998), Observed Episodic Warming at 86 and 100 km
 662 Between 1990 and 1997: Effects of Mount Pinatubo Eruption, *Geophys. Res. Lett.*, 25(4),
 663 497-500, doi: 10.1029/98GL00178

Author
Formatted: Font:(Default) Times New Roman, 12 pt

Author
Formatted: Font:(Default) Times New Roman, 12 pt

Author
Formatted: Font:(Default) Times New Roman, 12 pt

Author
Formatted: Font:(Default) Times New Roman, 12 pt

Author
Formatted: Font:(Default) Times New Roman, 12 pt

Author
Formatted: Font:(Default) Times New Roman, 12 pt

Author
Formatted: Font color: Custom Color(RGB(34,34,34)), (Asian) Chinese (PRC)

Author
Formatted: Font:(Default) Times New Roman

Author
Formatted: Font:(Default) Times New Roman, Not Bold

Author
Formatted: Font:(Default) Times New Roman

664 She, C. Y. (2000), Eight-year climatology of nocturnal temperature and sodium density in the
665 mesopause region (80 to 105 km) over Fort Collins, Co (41°N, 105°W), *Geophys. Res.*
666 *Let.*, 27(20), 3289-3292, doi: 10.1029/2000GL003825.

667 Smith, A. K. (2012), Global Dynamics of the MLT, *Surv. Geophys.*, 33(6), 1177–1230,
668 doi:10.1007/s10712-012-9196-9.

669 States, R. J., & Gardner, C. S. (1999). Structure of the mesospheric Na layer at 40°N latitude:
670 Seasonal and diurnal variations. *J. Geophys. Res.*, 104(D), 11,783-11,798. doi:
671 10.1029/1999JD900002.

672 Thorsen, D., S. J. Franke, and E. Kudeki (2000), Statistics of momentum flux estimation
673 using the dual coplanar beam technique, *Geophys. Res. Lett.*, 27, 3193–3196.

674 Tsuda, T., Y. Murayama, and M. Yamamoto (1990), Seasonal variation of momentum flux in
675 the mesosphere observed with the MU radar, *Geophys. Res. Lett.*, 17, 725–728.

676 Vincent, R. A., and I. M. Reid (1983), HF doppler measurements of mesospheric
677 gravity-wave momentum fluxes, *J. Atmos. Sci.*, 40(5), 1321-1333,
678 doi:10.1175/1520-0469(1983)040<1321:hdmomg>2.0.co;2.

679 Wu, Q., D. A. Ortland, T. L. Killeen, R. G. Roble, M. E. Hagan, H. L. Liu, S. C. Solomon, J.
680 Xu, W. R. Skinner, and R. J. Niecejewski (2008), Global distribution and interannual
681 variations of mesospheric and lower thermospheric neutral wind diurnal tide: 1.
682 Migrating tide, *J. Geophys. Res.*, 113(A), A05308, doi:10.1029/2007JA012542.

683 Xiong, J. G., W. Wan, B. Ning, and L. Liu (2004), First results of the tidal structure in the
684 MLT revealed by Wuhan Meteor Radar (30 degrees 40 ' N, 114 degrees 30 ' E), *J. Atmos.*
685 *Sol.-Terr. Phys.*, 66(6-9), 675-682, doi:10.1016/j.jastp.2004.01.018.

686 Xu, Jiyao, She, C. Y., Yuan Wei, Mertens Chris, Mlynczak Marty, Russell, James (2006),
687 Comparison between the temperature measurements by TIMED/SABER and lidar in the
688 midlatitude, *J. Geophys. Res.*, 11(A10), doi:10.1029/2005JA011439

689 Yi, F., C. Yu, S. Zhang, X. Yue, Y. He, C. Huang, Y. Zhang, and K. Huang (2009), Seasonal
690 variations of the nocturnal mesospheric Na and Fe layers at 30°N, *J. Geophys. Res.*, 114,
691 D01301, doi:10.1029/2008JD010344.

692 Yuan, T., et al. (2006), Seasonal variation of diurnal perturbations in mesopause region
693 temperature, zonal, and meridional winds above Fort Collins, Colorado (40.6°N, 105°W),
694 *J. Geophys. Res.*, 111, D06103, doi:10.1029/2004JD005486.

- 695 Yuan, T., She, C. Y., Kawahara Takuya D., Krueger, D. A. (2012), Seasonal variations of
696 midlatitude mesospheric Na layer and their tidal period perturbations based on full
697 diurnal cycle Na lidar observations of 2002–2008, *J. Geophys. Res.*, 117(D11),
698 doi:10.1029/2011JD017031.
- 699 Zahn, von, U., J. Hoffner, V. Eska, and M. Alpers (1996), The mesopause altitude: Only two
700 distinctive levels worldwide? *Geophys. Res. Lett.*, 23(2), 3231–3234,
701 doi:10.1029/96GL03041.
- 702 [Zhang, X., J. M. Forbes, and M. E. Hagan \(2010\), Longitudinal variation of tides in the MLT](#)
703 [region: 1. Tides driven by tropospheric net radiative heating, *J. Geophys. Res.*, 115,](#)
704 [A06316, doi:10.1029/2009JA014897.](#)
- 705 Zhao, G., L. Liu, W. Wan, B. Ning, and J. Xiong (2005), Seasonal behavior of meteor radar
706 winds over Wuhan, *Earth Planets and Space*, 57(1), 61–70, doi:10.1186/BF03351806.

Author

Formatted: EndNote Bibliography,
Justified, Indent: Left: 0 cm, Hanging:
4.26 ch, Space After: 0 pt, Line spacing:
1.5 lines, Adjust space between Latin and
Asian text, Adjust space between Asian
text and numbers

707 **Table 1.** Comparison of the GW zonal momentum flux (m^2/s^2) measured at different middle
 708 latitude lidar and radar stations.

Stations	Altitude/filter	Annual	Spring	Summer	Fall	Winter
USTC lidar (32°N, 117°E)	87 – 95 km 10min – 16hr	-0.08	1.4	-0.2	-0.3	-0.9
	87 – 95 km 10min – 2hr	-0.15	0.8	-0.9	-0.16	-0.6
SOR lidar (35°N, 107°W)	85 – 100 km 3min – 14hr	-1.2	~2	1.8	N/A	-1.7
CSU lidar (41°N, 105°W)	85 – 95 km 6min – 4hr	N/A	~0.1	N/A	~0.1	-0.7
MU Radar (35°N, 136°E)	65 – 85km 5min – 2 hr	N/A	~0	2.0	~0	-1.5

Author
Deleted: 7

Author
Deleted: 3

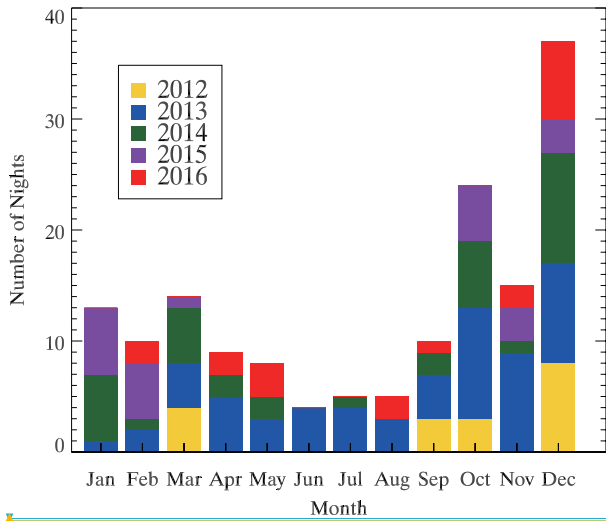
Author
Deleted: 5

Author
Deleted: 3

Author
Deleted: 8

Author
Deleted: 1.2

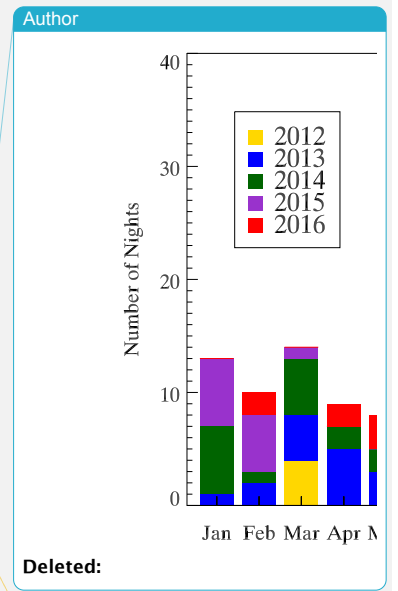
709



716

717

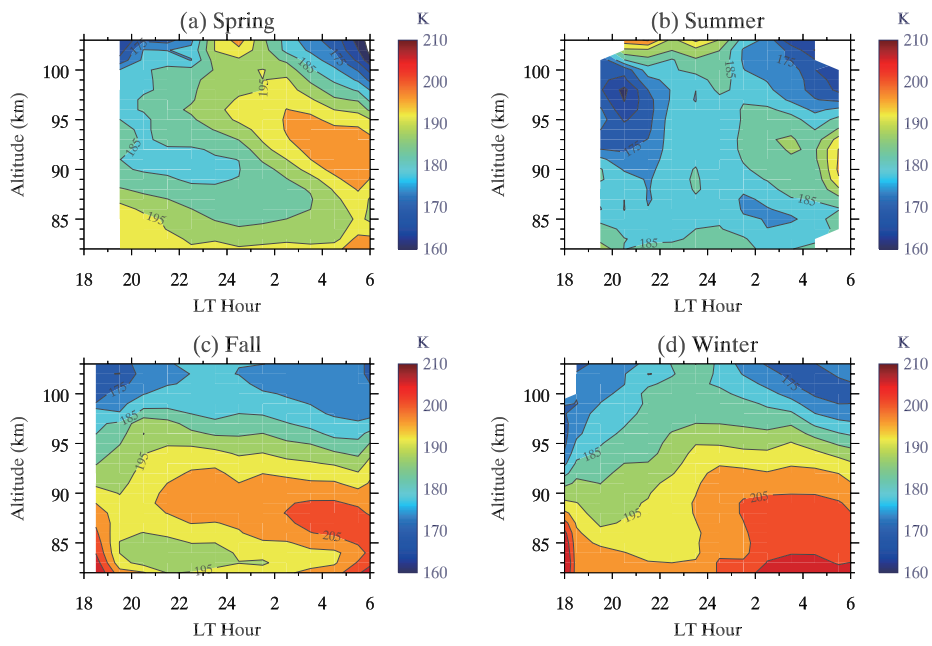
Figure 1. Histogram of number of nights with valid data observed by the USTC sodium lidar.



Deleted:

Unknown

Formatted: Font:(Default) Times New Roman, 12 pt



719

720 **Figure 2.** Lidar observed nighttime hourly mean temperature composite in (a) spring, (b)

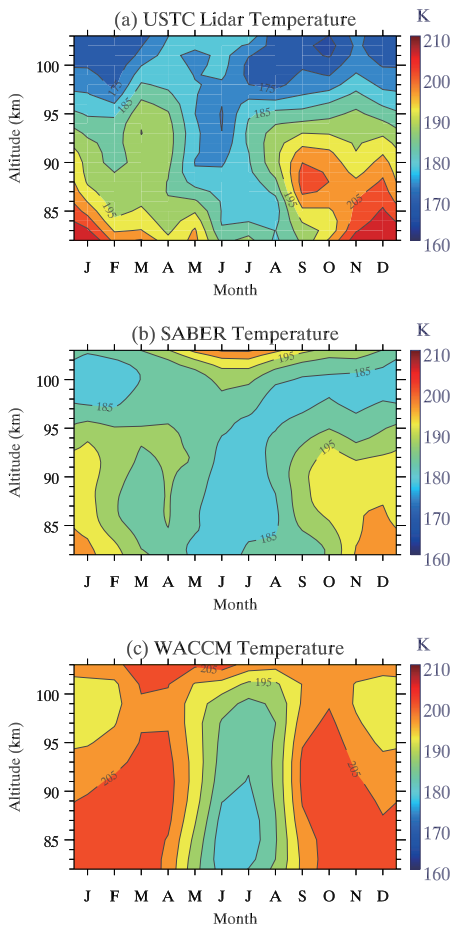
721 summer, (c) fall, and (d) winter.

Author

Deleted:

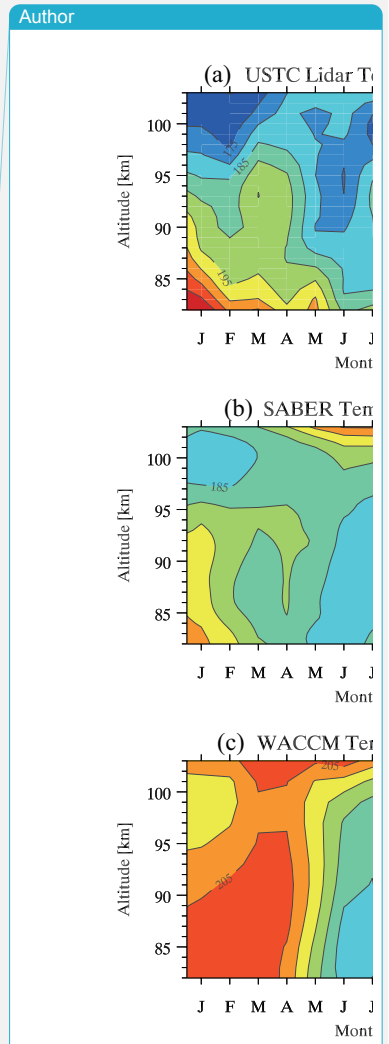
Unknown

Formatted: Font:(Default) Times New Roman, 12 pt



723

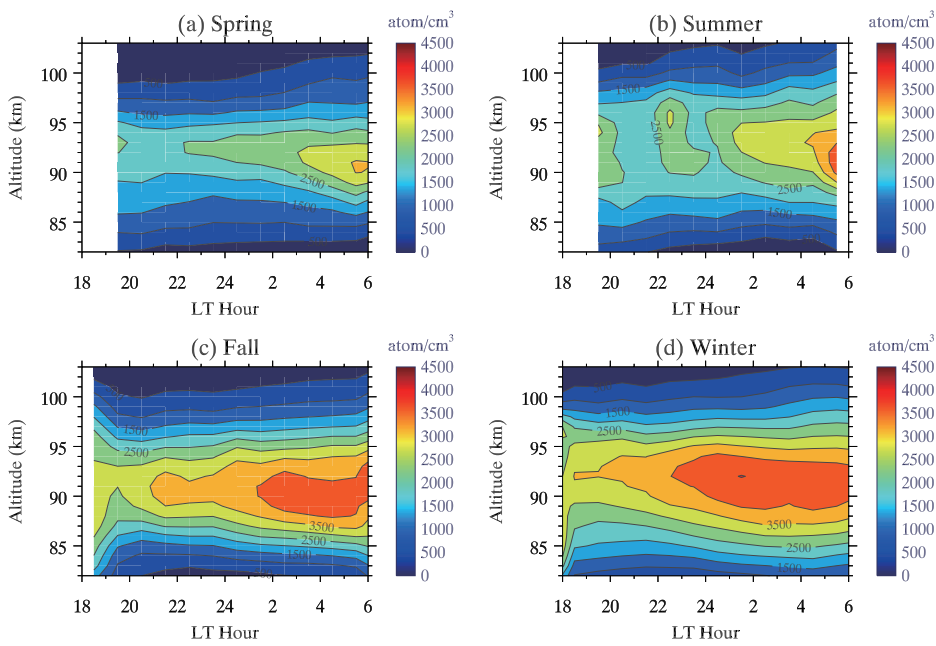
724 **Figure 3.** Monthly mean of mean temperature observed by (a) lidar, (b) SABER, and
 725 simulated by (c) WACCM.



Deleted:

Unknown

Formatted: Font:(Default) Times New Roman, 12 pt, Bold

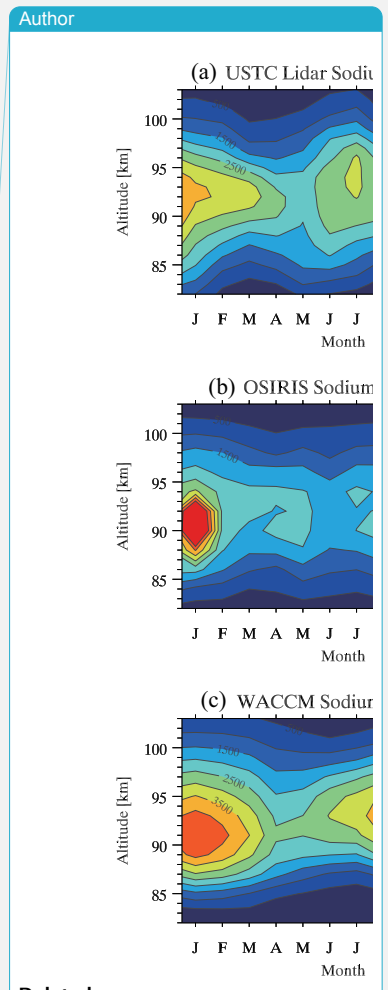
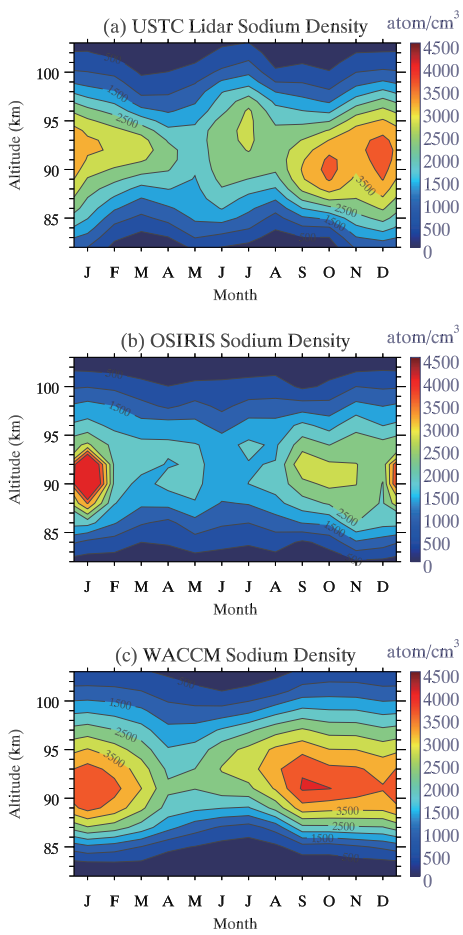


727

728 **Figure 4.** Same as Figure 2, but for sodium number density.

Author

Deleted:
Unknown
Formatted: Font:(Default) Times New Roman, 12 pt



Deleted:

Unknown

Formatted: Font:(Default) Times New Roman, 12 pt, Bold

730

731 **Figure 5.** Monthly mean of nightly mean sodium density observed by (a) lidar and (b) Odin/

732 OSIRIS, and simulated by (c) WACCM.

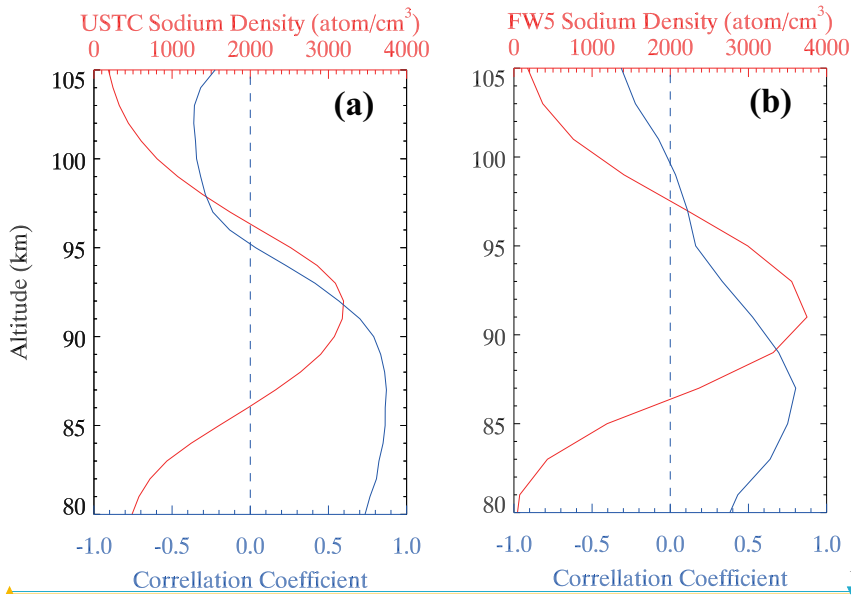


Figure 6.

734

735 The vertical profiles of correlation coefficient (blue) between composite temperature and
 736 relative sodium density perturbations, and annual mean sodium density (red), observed by
 737 lidar (left) and simulated by WACCM (right).

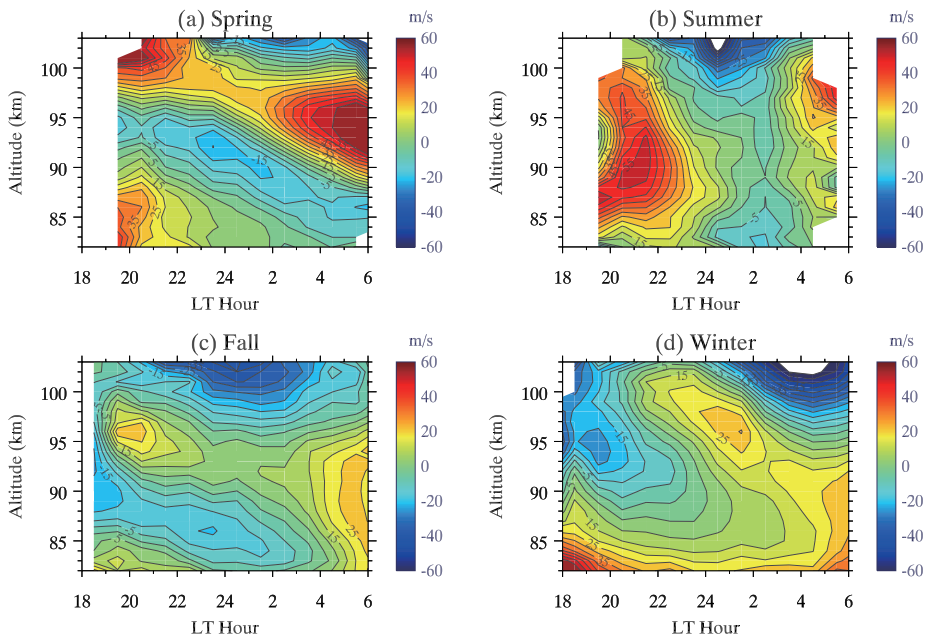
Unknown

Formatted: Font:(Default) Times New Roman, 12 pt

Author

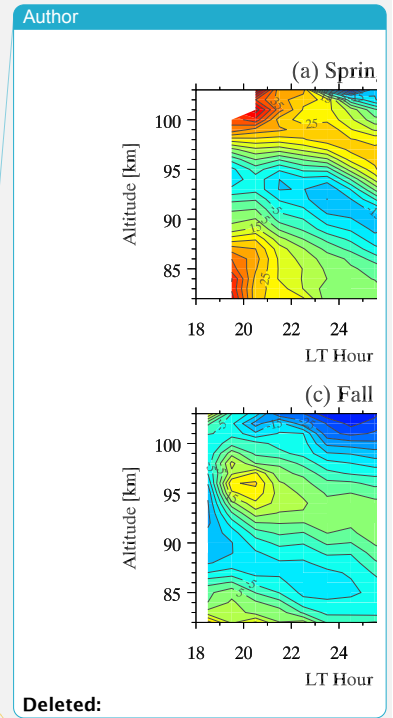
Deleted:

The deleted content contains two smaller versions of the plots from Figure 6. The top plot is for USTC Sodium I and the bottom plot is for FW5 Sodium Density. Both plots show Altitude (km) on the y-axis (80 to 105) and Correlation Coefficient on the x-axis (-1.0 to 1.0). They also include a top x-axis for Sodium Density (0 to 4000 for USTC, 0 to 3000 for FW5) and a vertical dashed line at Correlation Coefficient = 0.0.



740

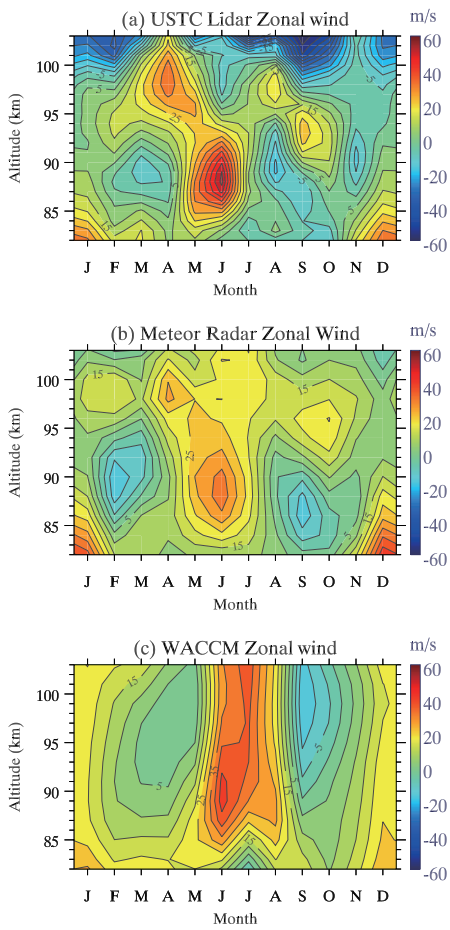
741 **Figure 7.** Same as Figure 2, but for zonal wind.



Deleted:

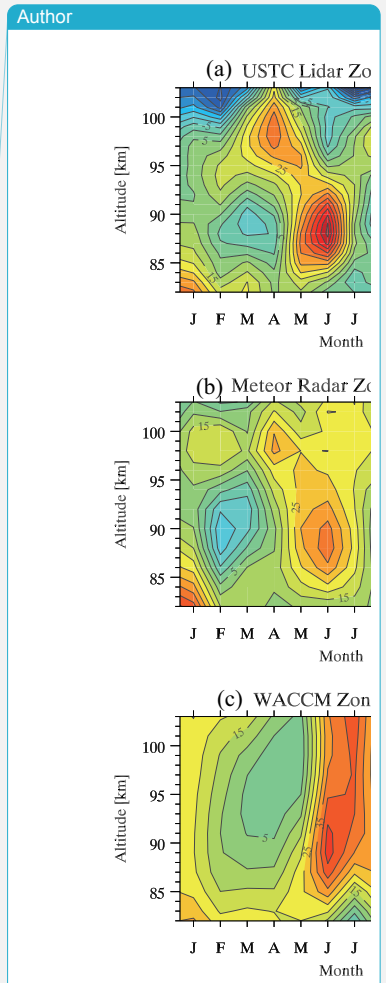
Unknown

Formatted: Font:(Default) Times New Roman, 12 pt



743

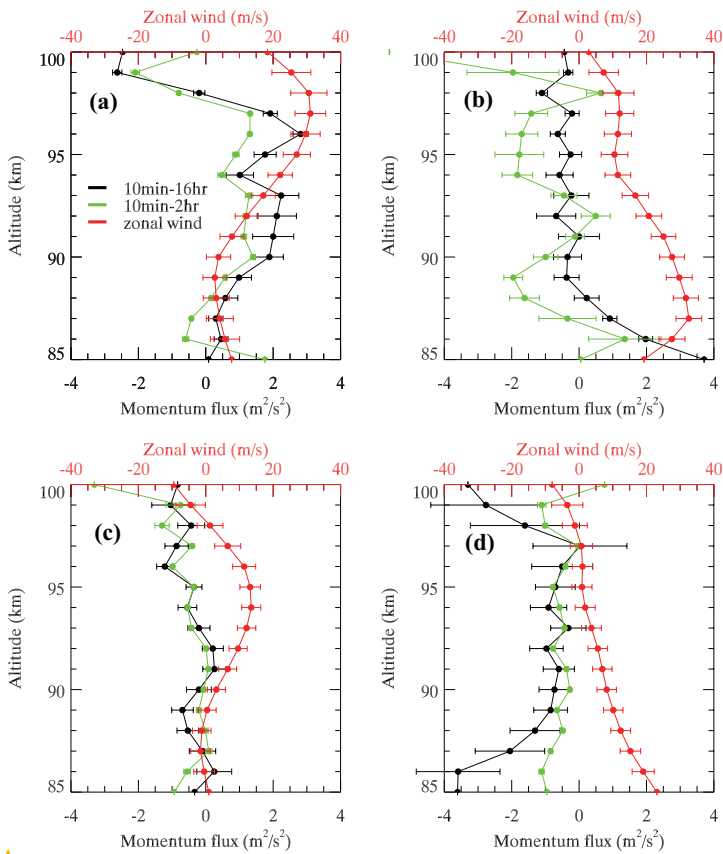
744 **Figure 8.** Monthly mean of nightly mean zonal wind observed by (a) lidar, (b) meteor radar,
 745 and simulated by (c) WACCM.



Deleted:

Unknown

Formatted: Font:(Default) Times New Roman, 12 pt



747

748 **Figure 9.** Comparison of seasonal mean of nightly mean zonal wind (red) and zonal
 749 momentum flux for 10min - 16hr (blue) and 10min - 2hr (green) observed by lidar in (a)
 750 spring, (b) summer, (c) fall, and (d) winter.

Author

Momentum flux

(a) Spring

Deleted:

Unknown

Formatted: Font:(Default) Times New Roman, 12 pt, Bold

Unknown

Formatted: Font:(Default) Times New Roman, 12 pt, Bold

Author

Deleted: (blue)